Research article

NMR IN BIOMEDICINE

Received: 29 May 2015, Revised: 9 September 2015, Accepted: 10 September 2015, Published online in Wiley Online Library

(wileyonlinelibrary.com) DOI: 10.1002/nbm.3425

Combining parallel detection of proton echo planar spectroscopic imaging (PEPSI) measurements with a data-consistency constraint improves SNR

Shang-Yueh Tsai[a,b], Yi-Cheng Hsu[c], Ying-Hua Chu[c], Wen-Jui Kuo[d] and Fa-Hsuan Lin[c,e]*

One major challenge of MRSI is the poor signal-to-noise ratio (SNR), which can be improved by using a surface coil array. Here we propose to exploit the spatial sensitivity of different channels of a coil array to enforce the *k*-space data consistency (DC) in order to suppress noise and consequently to improve MRSI SNR. MRSI data were collected using a proton echo planar spectroscopic imaging (PEPSI) sequence at 3 T using a 32-channel coil array and were averaged with one, two and eight measurements (avg-1, avg-2 and avg-8). The DC constraint was applied using a regularization parameter λ of 1, 2, 3, 5 or 10. Metabolite concentrations were quantified using LCModel. Our results show that the suppression of noise by applying the DC constraint to PEPSI reconstruction yields up to 32% and 27% SNR gain for avg-1 and avg-2 data with $\lambda = 5$, respectively. According to the reported Cramer–Rao lower bounds, the improvement in metabolic fitting was significant ($p < 0.01$) when the DC constraint was applied with $\lambda \geq 2$. Using the DC constraint with $\lambda = 3$ or 5 can minimize both root-mean-square errors and spatial variation for all subjects using the avg-8 data set as reference values. Our results suggest that MRSI reconstructed with a DC constraint can save around 70% of scanning time to obtain images and spectra with similar SNRs using $\lambda = 5$.

Keywords: proton echo planar spectroscopy imaging; data consistency; SNR; regularization

INTRODUCTION

MRSI can noninvasively elucidate the regional distributions of brain metabolites. Because both spatial and spectral information are measured together in MRSI, the acquisition time can be long. For example, one single 2D MRSI measurement with 3.5×3.5 mm^2 spatial resolution covering a single slice with 2 kHz bandwidth and 2 Hz spectral resolution takes about 30 min. The acquisition time of MRSI can be shortened by using fast switching gradient waveforms, such as EPI (1) and spiral (2), to encode spectral and spatial information efficiently (3–7). These fast MRSI techniques can reduce the scanning time from tens of minutes to a few minutes (8–10).

Alternatively, the MRSI acquisition time can be reduced by using parallel imaging (pMRI) techniques (3,4,11–13), where a surface coil array is used to detect NMR signals in parallel (14). The cost of the acceleration factor (R) is the reduced signal-to-noise ratio (SNR) as a consequence of reduced data samples and amplified noise in pMRI image reconstruction (15). While the latter cost can be partially alleviated by using prior information to regularize the reconstruction (16–18), the former cost is inevitable in accelerated acquisitions. Quantitatively, this $\sqrt{R}$-fold SNR reduction in R-fold accelerated pMRI becomes highly undesirable in SNR-hungry MRSI experiments. Noise correlation among phase array coils can be considered to improve the SNR in MRSI experiments (19).

Instead of reducing the acquisition time, simultaneously acquired pMRI data can be used to improve the MRSI data quality by reducing motion artifacts. This benefit is a consequence of pursuing the data consistency (DC) among channels

* *Correspondence to: F.-H. Lin, Institute of Biomedical Engineering, National Taiwan University, Taipei, Taiwan. E-mail: fhlin@ntu.edu.tw*

a *S.-Y. Tsai*
Graduate Institute of Applied Physics, National Chengchi University, Taipei, Taiwan

b *S.-Y. Tsai*
Research Center for Mind, Brain and Learning, National Chengchi University, Taipei, Taiwan

c *Y.-C. Hsu, Y.-H. Chu, F.-H. Lin*
Institute of Biomedical Engineering, National Taiwan University, Taipei, Taiwan

d *W.-J. Kuo*
Institute of Neuroscience, National Yang Ming University, Taipei, Taiwan

e *F.-H. Lin*
Department of Biomedical Engineering and Computational Science, Aalto University, Espoo, Finland

Abbreviations used: *SNR, signal-to-noise ratio; DC, data consistency; PEPSI, proton echo planar spectroscopic imaging; CRLB, Cramer–Rao lower bound; RMS, root mean square; pMRI, parallel imaging; ROI, region of interest; NAA, N-acetyl aspartate; tCr, total creatine; tCho, total choline; mI, myo-inositol; Glx, combination of glutamine and glutamate; NWS, non-water-suppressed; avg-8, eight averages; avg-2, two averages; avg-1, one average; CV, coefficient of variation; rSNR, relative SNR.*

of a coil array in either *k*-space (20–22), image domain (23) or coil sensitivity maps (24). Such a DC feature has also been applied to improve the pMRI reconstruction by considering the evolution of magnetization (25). Since the amount of data is not reduced, compared to the original MRSI reconstructions, the SNR may be even improved, if the noise suppression by

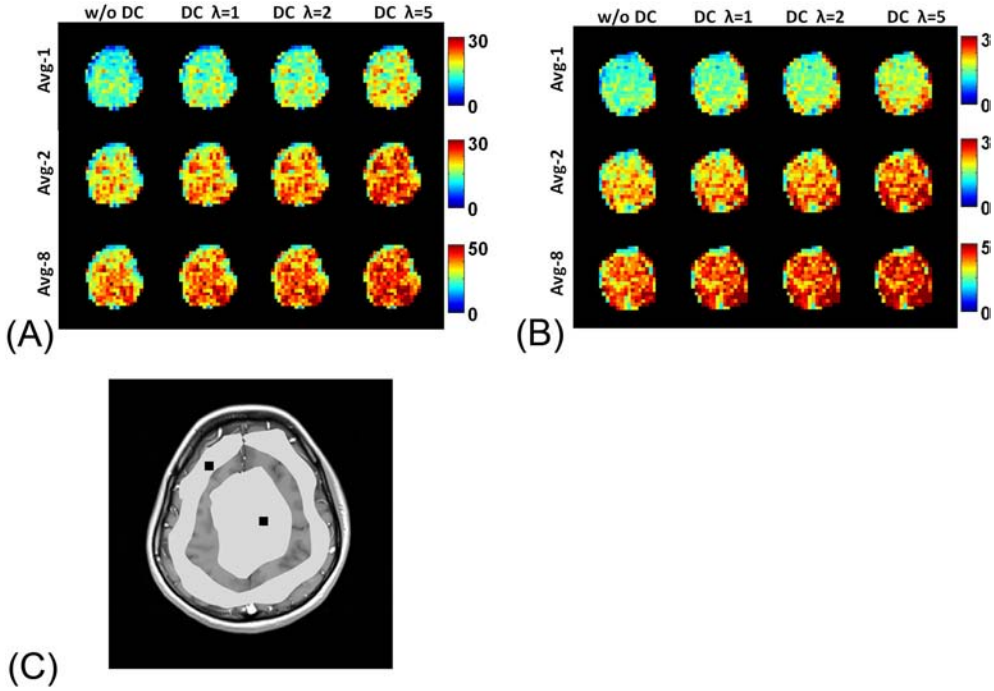

Figure 1. (A) SNR maps from avg-1, 2 and 8 data sets with DC reconstruction using constraints up to 5. (B) SNR maps from another subject. SNR is calculated based on the NAA peak. (C) The ROIs defined for the peripheral and central regions, and the location of representative spectra using one subject as an example.

Table 1. SNR of three ROIs from all subjects (mean ± standard deviation). Relative SNRs for avg-1, 2 and 8 data were calculated according to data without DC reconstruction. A pixel-wise paired Student *t*-test was performed for each subject. Statistical significance was marked if all subjects had $p < 0.01$ (*) and $p < 0.05$ (†)

		avg-1 w/o DC	avg-1 DC $\lambda=1$	avg-1 DC $\lambda=2$	avg-1 DC $\lambda=3$	avg-1 DC $\lambda=5$	avg-1 DC $\lambda=10$
Brain region	SNR	13.4 ± 0.5	14.9 ± 0.5*	15.7 ± 0.5*	16.3 ± 0.5*	17.6 ± 0.4*	18.1 ± 0.3*
	rSNR	–	1.12	1.17	1.22	1.32	1.35
Peripheral region	SNR	14 ± 1.4	16.2 ± 1.8†	17.1 ± 1.9*	17.9 ± 2*	19.4 ± 2.1*	20 ± 2.2*
	rSNR	–	1.16	1.23	1.28	1.39	1.43
Central region	SNR	14 ± 0.3	15.0 ± 0.3†	15.6 ± 0.3*	16.2 ± 0.4*	17.4 ± 0.4*	17.8 ± 0.6*
	rSNR	–	1.07	1.11	1.15	1.24	1.27
		avg-2 w/o DC	avg-2 DC $\lambda=1$	avg-2 DC $\lambda=2$	avg-2 DC $\lambda=3$	avg-2 DC $\lambda=5$	avg-2 DC $\lambda=10$
Brain region	SNR	18.6 ± 0.8	20.6 ± 0.8*	21.5 ± 0.8*	22.2 ± 0.8*	23.7 ± 0.7*	24.4 ± 0.5*
	rSNR	–	1.11	1.15	1.19	1.27	1.31
Peripheral region	SNR	19.5 ± 2.0	22.2 ± 2.4	23.3 ± 2.5†	24.2 ± 2.6*	25.7 ± 2.7*	26.6 ± 2.8*
	rSNR	–	1.14	1.20	1.24	1.32	1.36
Central region	SNR	19.6 ± 0.1	21.0 ± 0.1†	21.7 ± 0.2*	22.3 ± 0.2*	23.8 ± 0.3*	24.5 ± 0.6*
	rSNR	–	1.07	1.11	1.14	1.22	1.25
		avg-8 w/o DC	avg-8 DC $\lambda=1$	avg-8 DC $\lambda=2$	avg-8 DC $\lambda=3$	avg-8 DC $\lambda=5$	avg-8 DC $\lambda=10$
Brain region	SNR	35.5 ± 2.3	38.6 ± 2.3*	39.7 ± 2.3*	40.6 ± 2.2*	42.0 ± 2.1*	42.5 ± 1.8*
	rSNR	–	1.09	1.12	1.14	1.18	1.19
Peripheral region	SNR	37.1 ± 4.7	41.3 ± 5.1	42.6 ± 5.2†	43.5 ± 5.2†	45.0 ± 5.3*	45.4 ± 5.3*
	rSNR	–	1.11	1.15	1.17	1.21	1.23
Central region	SNR	37.2 ± 0.3	39.2 ± 0.3†	40.1 ± 0.3*	40.9 ± 0.2*	42.4 ± 0.1*	43.0 ± 0.4*
	rSNR	–	1.05	1.08	1.10	1.14	1.15

NMR IN BIOMEDICINE

pursuing the DC is more than the noise amplification in the reconstruction.

Here we propose to exploit the sensitivity information of a coil array to enforce the *k*-space DC in order to suppress noise and consequently to improve the SNR of MRSI. With *in vivo* experimental data at 3 T using a 32-channel coil array, we investigated the SNR gain because of using the DC constraint in reconstruction and examined the improvement in spectral fitting in metabolite concentration estimation.

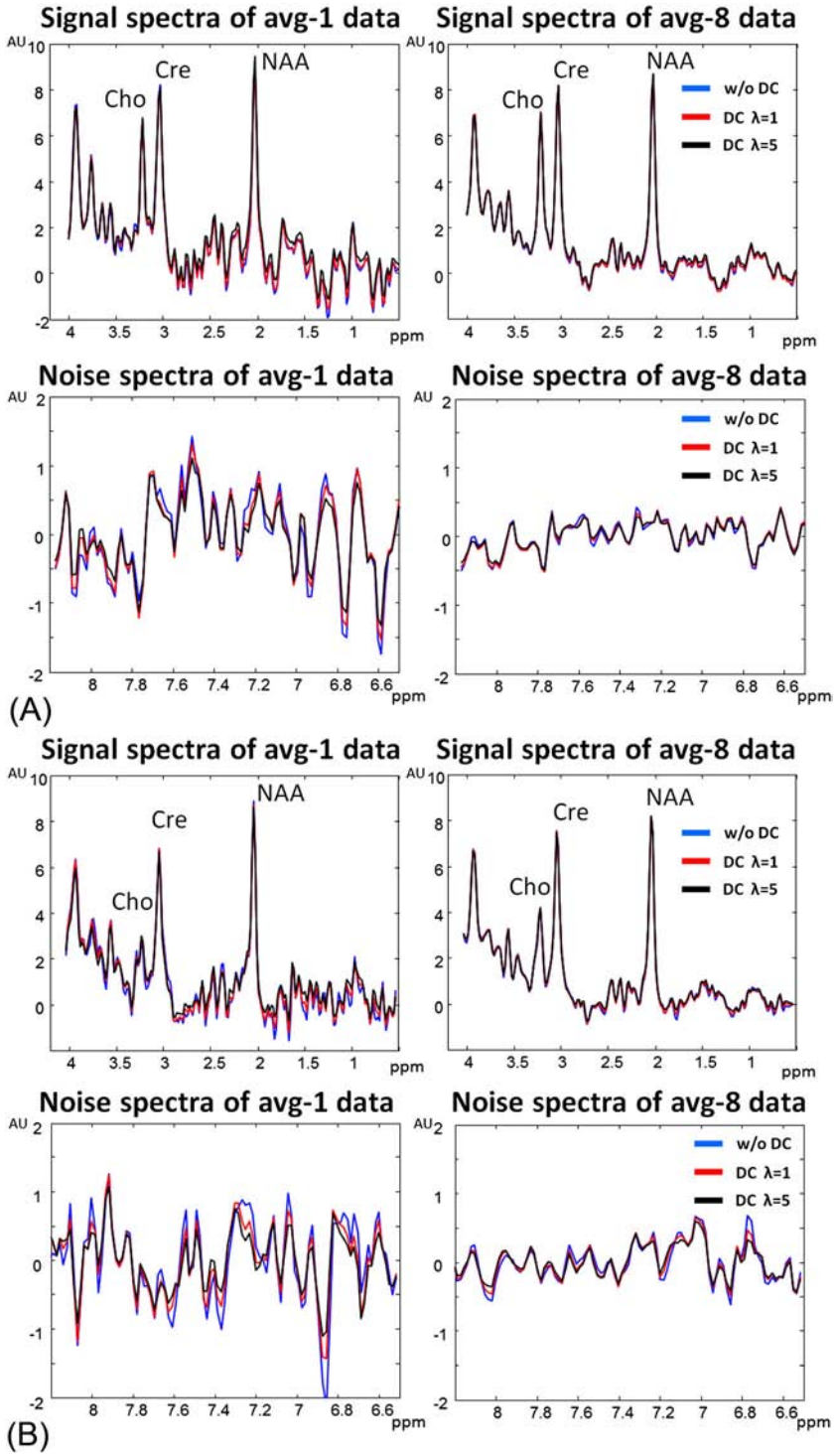

Figure 2. Representative spectra from (A) right central region of brain and (B) left frontal region of brain. Spectra from avg-1 and avg-8 data displayed in metabolite range 0.5 ppm–4 ppm and noise range 6.5 ppm–8.2 ppm. Noise inspected by baseline fluctuation on the noise spectra with DC processing using $\lambda = 1$ and $\lambda = 5$ is clearly reduced compared with that without DC reconstruction. In the signal spectra, the intensities of metabolic peaks are not changed by the DC process, by visual inspection. Note that the signal spectra [−2 to 10] and noise spectra [−2 to 2] are displayed using different vertical scales.

MATERIAL AND METHODS

Data acquisition

Proton echo planar spectroscopic imaging (PEPSI) was performed on six healthy volunteers (25 ± 5 years old) using a 3 T scanner (Skyra, Siemens Medical Solutions, Erlangen, Germany) with a 32-channel head coil array. All volunteers submitted written informed consent in accordance with the institutional review board approval. Before PEPSI acquisitions, T_1-weighted images, using a gradient echo sequence (T_R/T_E/flip angle, 250 ms/2.61 ms/70°; FOV, 256 × 256 mm^2; matrix, 128 × 128), were acquired for localizing the PEPSI slice and subsequent region of interest (ROI) selection. *In vivo* PEPSI data were acquired from a para-axial slice at the upper edge of the ventricles using the following parameters: $T_R = 2$ s, $T_E = 35$ ms, flip angle = 90°, 32 × 32 spatial matrix, FOV = 240 mm, slice thickness = 15 mm. Complete eight-slice outer volume suppression was applied along the perimeter of the brain to suppress the lipid signal. The PEPSI sequence used in this study has been described previously (5,26). The PEPSI scan was repeated eight times. Data from each repetition were saved individually. PEPSI data were averaged afterwards with one, two and eight measurements (avg-1, avg-2 and avg-8), representing spectra at different SNR levels. A non-water-suppressed (NWS) reference scan was acquired using only one average as the reference for phase correction, calibration of metabolic signal and estimation of the coil convolution kernel. The total scanning time was 10 min.

DC processing

The DC constraint was applied to individual measurement of PEPSI. These PEPSI data were then averaged to generate avg-1, avg-2 and avg-8 PEPSI data sets. It has been reported previously that each *k*-space data point of a coil can be expressed as a linear combination of the *k*-space data points from all coils in the vicinity of the chosen *k*-space data point (14,27). Among methods of pMRI reconstruction, SPIRiT is a method that synthesizes missing *k*-space data points by using one *k*-space lattice structure to linearly correlate neighboring *k*-space data points from all coils (28). Mathematically, such a relationship has a matrix representation

$$\mathbf{x} = \mathbf{G}\,\mathbf{x} \qquad [1]$$

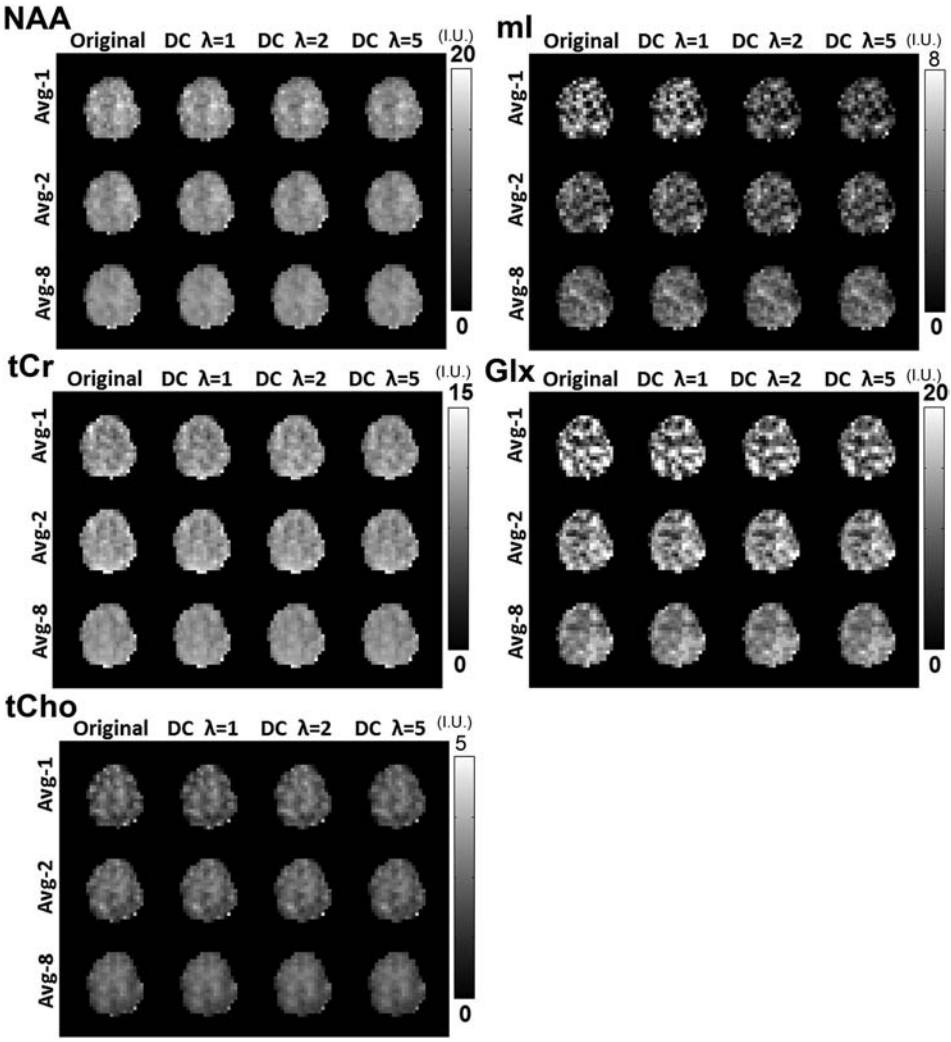

Figure 3. Concentration maps of NAA, tCr, tCho, mI and Glx from one subject.

where **x** denotes the concatenation of *k*-space data from all coils and **G** is a convolution kernel. Intuitively, the equation stands for the attempt to synthesize a *k*-space data point from its neighboring *k*-space data points. Importantly, the lattice structure required by SPIRiT prohibits the trivial solution of **G** as an identity matrix. Equation [1] describes the *k*-space DC constraint among channels of a coil array.

Reconstructing an MRI data set enforcing this DC constraint can be formulated as an optimization problem:

$$\hat{x} = \arg_x \min\left\{\lambda\left|\mathbf{Gx}-\mathbf{x}\right|_2^2 + \left|\mathbf{Sx}-\mathbf{y}\right|_2^2\right\} \quad [2]$$

where matrix **S** denotes a sampling matrix of *k*-space data. **y** is the acquired data across all channels of a coil array. λ is a regularization parameter adjusting the weight between two error terms: the DC term $|\mathbf{Gx}-\mathbf{x}|_2^2$ and the measurement consistency term $|\mathbf{Sx}-\mathbf{y}|_2^2$. We call the first error term the DC term to emphasize the property that the *k*-space data cross channels of a coil array should be related to each other by a convolution kernel, such as that defined in SPIRiT.

Practically, we first estimated the convolution kernel **G** and then reconstructed *k*-space data in each channel **x** by minimizing the cost function $|\mathbf{Sx}-\mathbf{y}|^2+\lambda|\mathbf{Gx}-\mathbf{x}|^2$. Again, **G** has a structure relating target *k*-space data locations and the associated *k*-space neighbors, as required by the SPIRiT formulation. Thus **G** cannot be degenerated to be the trivial solution of an identity matrix. The convolution kernel matrix **G** can be first estimated from a NWS scan around the water peak, which has a higher SNR. Subsequently, the solution minimizing the cost described by Equation [2] was calculated iteratively using a conjugated gradient method (29,30) based on the estimated **G**, the sampling matrix **S** and experimental data **y**. Unless otherwise noted, the regularization parameter λ was varied between 1, 2, 3, 5 and 10 in this study in order to avoid bias toward either error term. The size defining the neighborhood of the *k*-space data points (kernel size) was 2×2 in this study, because the difference between results using different kernel sizes was found to be relatively minor (31). Finally, the *k*-space data at each time point of the water-suppressed scan of each coil were reconstructed separately. The DC process did not change the data size or number of coils.

Post-processing

After DC processing, standard PEPSI post-processing steps were performed, including sinusoidal spatial filtering, time-domain filtering with a 2 Hz exponential filter, phase correction and even–odd echo editing (5,26). The reconstructed spectral width after even–odd echo editing was 1086 Hz, with 512 complex-number data points, yielding a spectral resolution of 2.1 Hz. The phase correction was performed before averaging data from individual coils to reduce the possible artifacts caused by partial phase cancellation.

In vivo localized spectra were quantified by the LCModel software package (http://s-provencher.com/pages/lcmodel.shtml). Spectra were fitted between 0.5 and 4 ppm. Metabolic signals were calibrated to NWS data using the water scaling method (32). In this study, five metabolites in the brain were quantified: N-acetyl aspartate (NAA), total creatine (tCr), including creatine and phosphocreatine, total choline (tCho), including glycerophosphocholine and phosphocholine, myo-inositol (mI) and a combination of glutamine and glutamate, denoted as Glx (33).

Spectral and error analysis

The performance of our reconstruction algorithm using the DC constraint was evaluated by calculating the SNR of the reconstructed spectra, which were calculated in the spectral domain at the NAA peak:

$$\mathrm{SNR} = \frac{\sum_{i\in n_{\mathrm{signal}}} s_i \Big/ n_{\mathrm{signal}}}{\sqrt{\sum_{j\in n_{\mathrm{noise}}} s_j{}^2 \Big/ n_{\mathrm{noise}}}} \quad [3]$$

Here, n_{signal} and n_{noise} represent the numbers of spectral points in the metabolite and in the noise ranges, respectively. The range for metabolite was defined as 0.1 ppm symmetrical around the peak maximum, whereas the range for noise was calculated between 7.5 ppm and 8.5 ppm. s*j* indicates the real part of the reconstructed spectrum with the spectral index *j*. The relative SNR (rSNR), the ratio between the SNR of the reconstruction with and without the DC constraint, was calculated as the following:

$$\mathrm{rSNR} = \frac{\mathrm{SNR_{dc}}}{\mathrm{SNR_{w/o\ dc}}} \quad [4]$$

The Cramer–Rao lower bound (CRLB), provided by LCModel, was used as the error metric for metabolite quantification. It is the lowest bound of the standard deviation of the estimated metabolite concentration. Expressed in percentage concentration, the CRLB can be used as an indicator of the reliability for metabolic concentration quantification. The CRLB for each metabolite is typically used to quantify the goodness of fit in LCModel. To facilitate the presentation of metabolite maps and the comparison between metabolite concentrations, spectroscopic image voxels with CRLB > 50% and spectral linewidth > 0.1 ppm were rejected.

To evaluate the spatial uniformity of quantified metabolite concentrations for each subject, the coefficient of variation (CV), which represents the spatial variation of metabolite concentrations within the ROI, was calculated as the standard deviation divided by the mean. The values were displayed as percentages.

The metabolite concentration errors were evaluated in a pixel-by-pixel manner based on the root mean square difference:

$$\text{RMS error } (\%) = \sqrt{\sum_i \left(\frac{C^{\mathrm{ref}}{}_i - C^{\mathrm{R}}{}_i}{C^{\mathrm{ref}}{}_i}\right)^2 \Big/ N}, \quad [5]$$

where C^{ref} is the concentration from the avg-8 data set without using the DC constraint in the reconstruction, C^{R} is the concentration from the PEPSI data with avg-1, avg-2, avg-4 or without DC constraint and *N* is the total number of image voxels in the ROI. The subscript *i* indicates the spatial location of the image voxel.

To investigate the regional differences in the PEPSI reconstruction with the DC constraint, we manually selected three ROIs in the anatomical image: the peripheral brain region, the central brain region and the whole brain region. The RMS error and SNR at these three ROIs were calculated for each subject. The SNR, linewidth and CRLB for the PEPSI reconstruction with the DC constraint were compared with those without the DC constraint using Student's *t*-test at each image pixel.

RESULTS

Figure 1 shows the NAA SNR maps from two subjects. We found that the SNR increased after applying the DC constraint to avg-1, avg-2 and avg-8 data sets. SNR and rSNR are listed in Table 1. For reconstructions without using the DC constraint, the SNR gain between avg-2 and avg-1 was 1.39, and the gain between avg-8 and avg-2 was 1.9. This matches the theoretical SNR gain of 1.41 and 2 based on the number of measurements. The overall SNR improvement by using the DC constraint with $\lambda = 5$ was 32%, 27% and 18% in avg-1, avg-2 and avg-8 data sets, respectively. SNR gains increase to 35%, 31% and 19% in avg-1, avg-2 and avg-8 data when = 10. The SNR gains are statistically significant ($P < 0.01$) with $\lambda \geq 2$ in the avg-1 data set and with $\lambda \geq 3$ in the avg-2 data set. Significantly higher SNR gain was found in the peripheral region than in the central region ($p < 0.01$) for all subjects. The averaged line width (across all image voxels) in the brain region of a representative subject was 0.057 ppm, with a standard deviation of 0.009 ppm. The difference in the line width for data reconstructed with and without the DC constraint was not statistically significant ($p > 0.5$) at three ROIs in all subjects.

Figure 2 shows the spectra from two representative voxels located in the white and gray matter in the metabolic range between 0.5 and 4 ppm and in the noise range between 6.5 and 8 ppm. Major metabolite peaks were clearly identified in all spectra. The noise level was reduced by using the DC constraint for both avg-1 and avg-8 data sets. The NAA, tCr and tCho signals were not affected by using the DC constraint even using $\lambda = 5$. Note that peaks around 2.2 ppm in the avg-1 data reconstructed with the DC constraint, potentially from the Glx, showed similar shapes to those in the avg-8 data.

In vivo metabolite concentration maps of NAA, tCr, tCho, mI and Glx with their corresponding CRLB maps from one subject are shown in Figures 3 and 4. Metabolic maps were relatively

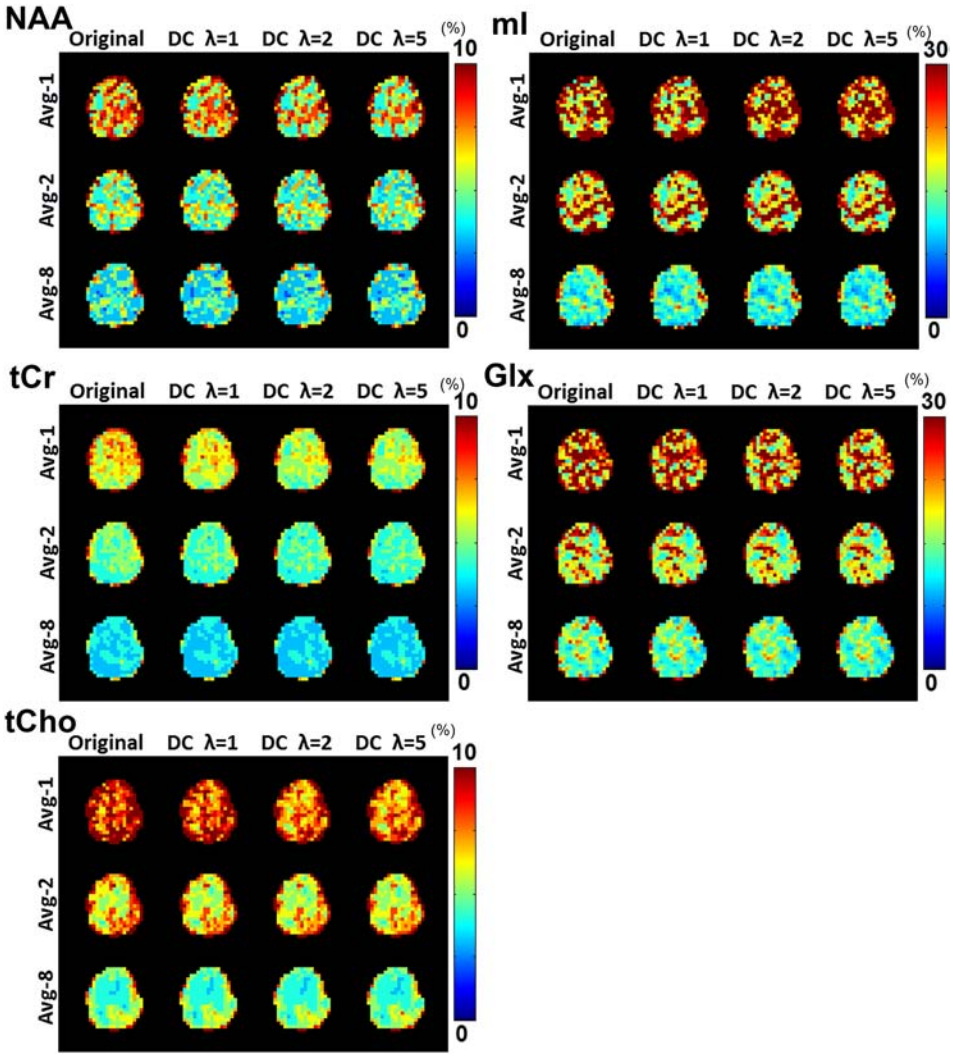

Figure 4. CRLB maps of NAA, tCr, tCho, mI and Glx from one subject.

NMR IN BIOMEDICINE

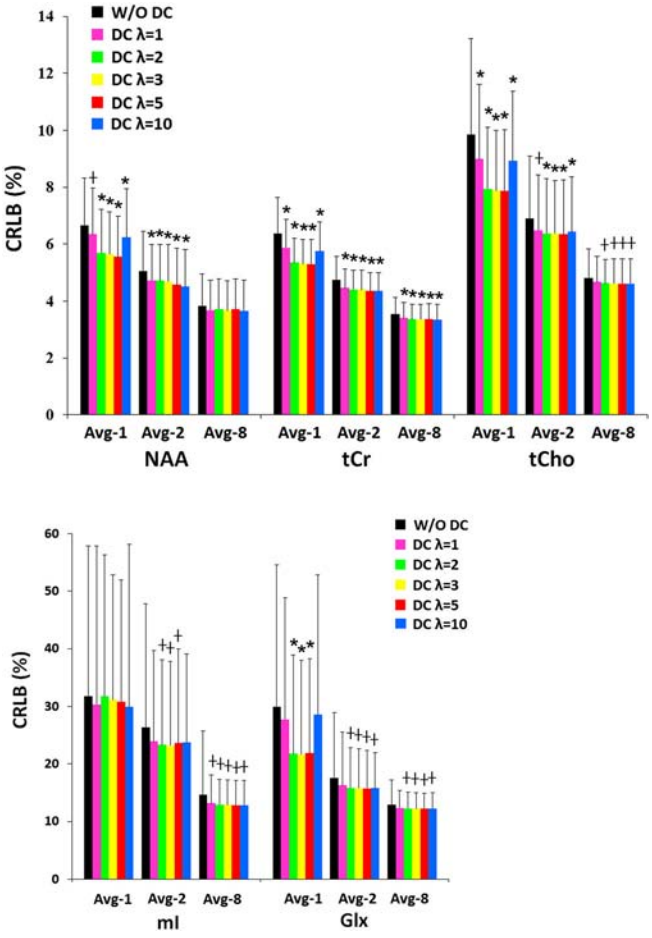

Figure 5. Averaged CRLBs with standard deviations for NAA, tCr, tCho, mI and Glx. Results are calculated over the brain region in the slice from one subject. Statistical significances by pixel-wise paired Student *t*-test are shown above each bar (* $p < 0.01$, † $p < 0.05$).

uniform when more measurements were averaged. The improved spatial uniformity after using the DC constraint was observed for NAA, tCr and tCho in avg-1 data and for mI and Glx in all data sets. The reduction of CRLB values because of using the DC constraint was observed on the corresponding data sets. Quantitative comparison of the CRLBs for five metabolites from the same subject is shown in Figure 5. Using the DC constraint reduced CRLB for all metabolites in avg-1, avg-2 and even avg-8 data sets, except mI in the avg-1 data set (Fig. 5). CRLBs were significantly reduced by using the DC constraint with $\lambda \geq 2$ for NAA, tCr and tCho in avg-1 and avg-2 data sets ($p < 0.01$). For Glx, CRLBs decreased from $29.9 \pm 24.6\%$ to $21.9 \pm 16.5\%$ and from $17.6 \pm 11.3\%$ to $15.6 \pm 6.6\%$ for the avg-1 data set ($P < 0.01$) and avg-2 data set ($P < 0.05$). More specifically, the lowest CRLBs were found with $\lambda = 3$ or 5. For the avg-8 data set, the CRLB was significantly reduced for tCr ($p < 0.01$), tCho, mI and Glx ($p < 0.05$). Reliable fitting of a metabolite led to less variation in metabolite quantification for all subjects, as shown by the CV (Fig. 6). Among avg-1, avg-2 and avg-8 data sets, avg-8 data sets showed the lowest CV. For avg-1 and avg-2 data sets, CVs with $\lambda = 3$ or 5 were closest to those from the avg-8 data set for each metabolite. Overall, the CVs had similar tendency to CRLBs (Fig. 5). RMS errors of metabolite concentrations based on the avg-8 data set without using the DC constraint are summarized in Table 2. Larger RMS errors were found in the avg-1 data set than in the avg-2 data set for all metabolites. Means and standard deviations of averaged concentrations from the whole brain region from all subjects are summarized in Table 3. A tendency of lower mean concentrations using larger λ can be found for avg-1, avg-2 and avg-8 data sets. For reference avg-8 data sets, the differences of mean concentrations using λ from 1 to 5 are less than 2% for all metabolites. In general, using the DC constraint can reduce both RMS errors and CV, and using $\lambda = 3$ or 5 can give the lowest RMS errors and CV. Larger RMS errors were found in the peripheral region than in the central region.

DISCUSSION

We proposed an MRSI reconstruction algorithm enforcing the *k*-space DC among channels of a coil array such that noise disturbing such a consistency is suppressed. In contrast to the optimal reconstruction of coil array images (34), our method does not require explicit estimates of coil sensitivity maps. For MRSI, especially fast MRSI methods such as PEPSI, the NWS scan is routinely collected as a reference for phase correction and concentration calibration. Thus we consider that using NWS data to estimate convolution kernels is practical. The suppression of noise by applying the DC constraint to PEPSI reconstruction yields up to 32% and 27% SNR gain for avg-1 and avg-2 data sets with $\lambda = 5$. Even for the data set with eight averages

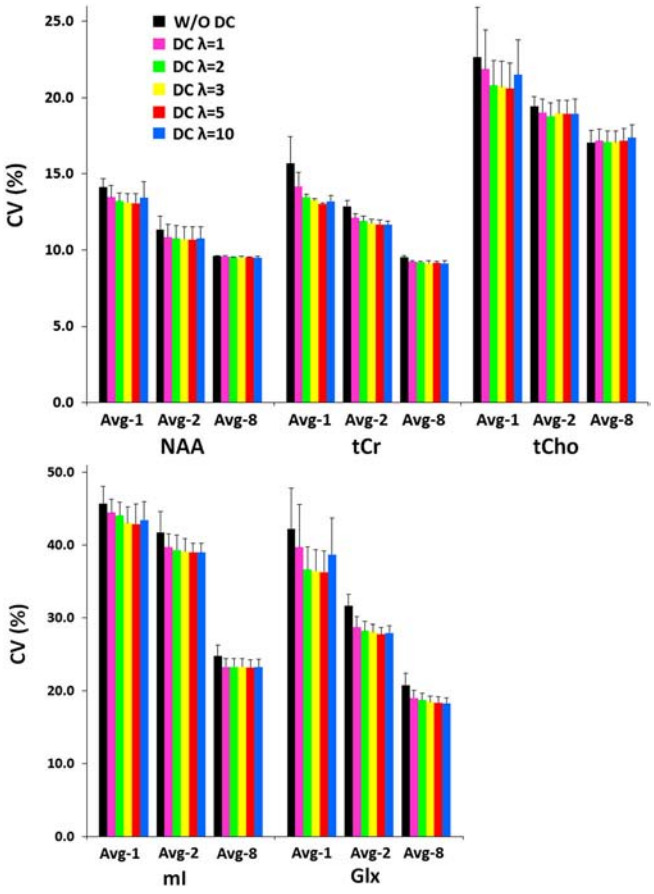

Figure 6. Averaged CVs with standard deviation for NAA, tCr, tCho, Mi and Glx. Results are calculated over the brain region in the slices from all subjects.

Table 2. RMS errors (%) of three ROIs from all subjects (mean ± standard deviation). Avg-8 data without DC reconstruction was used as reference standard

		avg-1 w/o DC	avg-1 DC $\lambda=1$	avg-1 DC $\lambda=2$	avg-1 DC $\lambda=3$	avg-1 DC $\lambda=5$	avg-1 DC $\lambda=10$	avg-2 w/o DC	avg-2 DC $\lambda=1$	avg-2 DC $\lambda=2$	avg-2 DC $\lambda=3$	avg-2 DC $\lambda=5$	avg-2 DC $\lambda=10$
Brain region	NAA	6.0 ± 0.4	5.7 ± 0.5	5.2 ± 0.1	5.1 ± 0.1	5.1 ± 0.1	5.7 ± 0.3	4.3 ± 0.3	4.1 ± 0.3	4.0 ± 0.3	4.0 ± 0.3	4.0 ± 0.3	4.3 ± 0.4
	tCr	7.1 ± 0.3	6.3 ± 0.2	5.9 ± 0.2	5.6 ± 0.2	5.3 ± 0.2	7.3 ± 2.6	5.5 ± 0.6	5.1 ± 0.4	4.7 ± 0.4	4.6 ± 0.4	4.3 ± 0.4	4.5 ± 0.4
	tCho	10.1 ± 0.1	9.3 ± 0.4	8.6 ± 0.2	8.1 ± 0.3	7.5 ± 0.6	9.2 ± 3.8	7.3 ± 0.3	6.7 ± 0.3	6.5 ± 0.3	6.3 ± 0.5	6.0 ± 0.6	6.2 ± 1.2
	mI	22.5 ± 2.0	20.8 ± 2.5	19.2 ± 0.7	19.0 ± 1.2	18.8 ± 1.6	18.5 ± 1.1	17.4 ± 0.2	16.4 ± 0.3	16.2 ± 0.3	16 ± 0.3	16.1 ± 0.5	16.4 ± 0.6
	Glx	20.0 ± 4.7	18.7 ± 4.5	17.3 ± 2.5	17.2 ± 2.4	17.0 ± 2.0	17.8 ± 2.6	13.9 ± 0.4	12.9 ± 0.4	12.6 ± 0.3	12.5 ± 0.1	12.2 ± 0.3	12.1 ± 0.7
Peripheral region	NAA	6.3 ± 0.1	5.9 ± 0.3	5.2 ± 0.6	5.1 ± 0.6	5.0 ± 0.5	5.9 ± 0.5	4.5 ± 0.4	4.3 ± 0.4	4.3 ± 0.4	4.2 ± 0.3	4.1 ± 0.4	4.4 ± 0.4
	tCr	7.7 ± 0.2	6.7 ± 0.1	6.6 ± 0.3	6.2 ± 0.2	5.8 ± 0.1	7.6 ± 1.9	6.4 ± 1.2	5.8 ± 1.1	5.5 ± 1.1	5.3 ± 1.0	5 ± 0.9	5.1 ± 0.7
	tCho	11.6 ± 0.2	10.5 ± 0.6	9.5 ± 0.1	9.0 ± 0.3	8.3 ± 0.8	9.8 ± 4.5	8.2 ± 0.3	7.5 ± 0.4	7.3 ± 0.4	7.0 ± 0.6	6.6 ± 0.7	6.4 ± 1.2
	mI	24.4 ± 1.6	22.7 ± 2.6	19.5 ± 1.0	19.1 ± 0.3	18.8 ± 0.6	19.4 ± 1.9	16.9 ± 0.3	15.5 ± 0.5	15.5 ± 0.1	15.2 ± 0.1	15.2 ± 0.1	15.5 ± 0.1
	Glx	19.6 ± 4.1	18.2 ± 4.8	16.5 ± 2.1	16.4 ± 1.9	16.2 ± 1.4	17.2 ± 2.7	14.9 ± 0.4	13.5 ± 0.4	13.3 ± 0.6	13.2 ± 0.7	13.0 ± 1.3	12.8 ± 1.9
Central region	NAA	6.1 ± 0.6	5.8 ± 0.8	5.7 ± 0.8	5.6 ± 0.7	5.5 ± 0.4	5.7 ± 0.3	3.9 ± 0.2	3.7 ± 0.1	3.7 ± 0.1	3.7 ± 0.1	3.8 ± 0.1	4.4 ± 0.5
	tCr	6.2 ± 0.1	5.7 ± 0.4	5.1 ± 0.1	4.9 ± 0.1	4.7 ± 0.2	7.1 ± 3.2	4.0 ± 0.7	3.7 ± 0.7	3.5 ± 0.6	3.4 ± 0.5	3.4 ± 0.4	4.0 ± 0.3
	tCho	8.0 ± 1.5	7.5 ± 1.2	7.2 ± 0.9	7.0 ± 0.9	6.5 ± 0.6	8.3 ± 2.5	5.9 ± 0.7	5.8 ± 0.4	5.7 ± 0.3	5.5 ± 0.1	5.3 ± 0.2	5.8 ± 1.1
	mI	20.2 ± 2.5	19.2 ± 2.7	19.5 ± 3.0	19.4 ± 3.3	19.3 ± 3.3	17.9 ± 0.9	17.9 ± 1.0	17.2 ± 0.9	16.8 ± 1.1	16.8 ± 1.2	16.9 ± 1.3	17.5 ± 1.4
	Glx	20.7 ± 4.7	19.3 ± 3.5	19.2 ± 3.4	19.1 ± 3.2	19.0 ± 3.0	18.8 ± 1.8	12.5 ± 0.5	12.0 ± 1.0	11.9 ± 0.8	11.8 ± 0.7	11.7 ± 0.6	11.9 ± 0.6

(avg-8), with an SNR of 35, there is still another 18% SNR gain by applying the DC constraint in the reconstruction. According to the reported CRLBs, CVs and RMS errors, the performance of metabolic fitting is optimized when the DC constraint is applied with $\lambda = 3$ or 5, where the SNR gain ranged between 22% and 32% for the avg-1 data set and between 19% and 27% for the avg-2 data set.

The contribution of SNR improvement using the DC constraint in metabolite quantification can be specifically observed in Glx estimation using the avg-1 and avg-2 data sets (Fig. 5). There are fewer voxels showing unreliable Glx fitting by LCModel, presented as black blobs, on the Glx maps using the DC constraints compared to those without DC constraints (Fig. 3). Reliable fitting results in smooth metabolite distributions in the brain (Fig. 6). However, spectral fitting of *in vivo* spectra are affected by many factors including SNR, linewidth, overlapping of metabolites and macromolecules in the baseline. Fitting reliabilities for metabolites vary according to the effect of these factors on the spectral line shape of the metabolite. In general, quantifications of NAA, tCr and tCho are considered relatively stable compared with mI and Glx, because mI and Glx have complex spectral shapes. Even with 30% SNR improvement in avg-1 data, it is suggested to use avg-8 data for quantification of Glx and mI. CRLBs on the avg-8 data set were not significantly different before and after using the DC constraint, indicating that the SNR on the avg-8 data set was already sufficient for metabolite quantification after multiple averages. In this study, we used the avg-8 data set as the relative gold standard. While the avg-8 data set cannot represent the true metabolite values, the overall CRLBs are less than 5% for NAA, tCr and tCho, and less than 15% for mI and Glx. This suggested that the avg-8 data set already had high SNR. Therefore, the avg-8 data set can suitably serve as the comparing reference.

Increasing DC constraints from $\lambda = 5$ to $\lambda = 10$ leads to only additional 3% SNR gain, but this raised CRLBs (Fig. 5), CVs (Fig. 6) and RMS errors (Table 2) in the avg-1 and avg-2 data sets. One possible explanation is that the results of using the DC constraint to suppress the noise at the cost of the marginally reduced signal (metabolite peak) are similar to the advantage of using *a priori* information to regularize parallel functional MRI reconstruction (35). Yet our method does not need to explicitly specify the prior. Choosing a larger regularization parameter ($\lambda = 10$) can bias the reconstruction into the null space of **G**, and in turn can lead to potential reduction of spectral peaks. Spectral fitting accounts for not only SNR but also other effects such as baseline attenuation caused by macromolecules, and metabolite spectral peaks overlapping. Therefore, when a stronger DC constraint ($\lambda = 10$) is used, baseline fluctuation can be further reduced but may also increase errors on the quantification of metabolite concentration (Fig. 6 and Table 2). The attenuation of signal, which leads to reduced bias metabolite concentrations, can be found at larger regularization parameters ($\lambda = 10$) (Table 3). Using $\lambda \leq 5$ causes less than 2% bias difference in concentrations (Table 3).

The decrease in the RMS error on avg-1 and avg-2 data sets with the DC constraint can be attributed to the improved spectral fitting, which lowers the spatial variation (Fig. 6) and indeed gives concentration estimates close to the reference values (Table 2). This implies that the PEPSI reconstruction with the DC constraint using a proper regularization parameter ($\lambda = 3$ or 5) can significantly reduce noise to achieve reliable spectral fitting without effectively attenuating the signal. One should notice

Table 3. Means and standard deviations of concentrations for avg-1, avg-2 and avg-8 data sets from whole brain region from six subjects

	avg-1 w/o DC	avg-1 DC $\lambda=1$	avg-1 DC $\lambda=2$	avg-1 DC $\lambda=3$	avg-1 DC $\lambda=5$	avg-1 DC $\lambda=10$
NAA	13.23 ± 0.08	13.19 ± 0.11	13.03 ± 0.21	12.94 ± 0.25	12.81 ± 0.31	12.21 ± 0.34
tCr	10.33 ± 0.59	10.16 ± 0.62	10.39 ± 0.3	10.26 ± 0.32	10.05 ± 0.37	9.00 ± 0.68
tCho	2.55 ± 0.35	2.51 ± 0.34	2.58 ± 0.25	2.54 ± 0.25	2.46 ± 0.25	2.18 ± 0.33
mI	4.01 ± 0.17	3.91 ± 0.19	3.70 ± 0.11	3.69 ± 0.06	3.62 ± 0.14	3.41 ± 0.23
Glx	12.43 ± 0.22	12.42 ± 0.15	12.24 ± 0.31	12.17 ± 0.26	12.06 ± 0.21	11.13 ± 0.32
	avg-2 w/o DC	avg-2 DC $\lambda=1$	avg-2 DC $\lambda=2$	avg-2 DC $\lambda=3$	avg-2 DC $\lambda=5$	avg-2 DC $\lambda=10$
NAA	13.04 ± 0.26	12.99 ± 0.26	12.95 ± 0.28	12.88 ± 0.29	12.79 ± 0.27	12.38 ± 0.40
tCr	10.50 ± 0.17	10.38 ± 0.22	10.30 ± 0.23	10.22 ± 0.23	10.04 ± 0.26	9.6 ± 0.29
tCho	2.56 ± 0.22	2.53 ± 0.22	2.51 ± 0.22	2.49 ± 0.22	2.44 ± 0.22	2.31 ± 0.22
mI	3.51 ± 0.10	3.52 ± 0.11	3.50 ± 0.10	3.47 ± 0.10	3.47 ± 0.09	3.22 ± 0.11
Glx	12.73 ± 0.05	12.8 ± 0.06	12.73 ± 0.06	12.62 ± 0.06	12.5 ± 0.09	11.84 ± 0.17
	avg-8 w/o DC	avg-8 DC $\lambda=1$	avg-8 DC $\lambda=2$	avg-8 DC $\lambda=3$	avg-8 DC $\lambda=5$	avg-8 DC $\lambda=10$
NAA	12.89 ± 0.30	12.89 ± 0.31	12.87 ± 0.32	12.84 ± 0.33	12.8 ± 0.34	12.68 ± 0.36
tCr	10.00 ± 0.24	9.93 ± 0.27	9.89 ± 0.28	9.86 ± 0.28	9.82 ± 0.27	9.65 ± 0.29
tCho	2.41 ± 0.17	2.40 ± 0.17	2.39 ± 0.18	2.38 ± 0.17	2.36 ± 0.17	2.31 ± 0.17
mI	3.9 ± 0.10	3.97 ± 0.09	3.98 ± 0.08	3.97 ± 0.08	3.95 ± 0.08	3.89 ± 0.08
Glx	12.68 ± 0.61	12.59 ± 0.57	12.55 ± 0.55	12.51 ± 0.56	12.42 ± 0.55	12.21 ± 0.56

that reconstructions using the DC constraint only reduced the noise level without changing the noise spectra (Fig. 2). Therefore, the spectral shapes and line widths did not change significantly after applying the DC constraint. As for spatial resolution, the DC process uses a calibration kernel in *k*-space, and the *k*-space size is not changed after the DC process, so the nominal spatial resolution should remain the same. Note that reconstructions using the DC constraint caused less than 3% RMS error difference in metabolite concentrations for the avg-1 and avg-2 data sets, except mI. There are bias RMS errors higher than 3% between avg-1, avg-2 data sets and avg-8 data sets.

One limit of our method is closely related to the accuracy of the kernel describing the linear relationship between one *k*-space data point and the collection of other *k*-space data points in its vicinity from other RF channels. It is not surprising that erroneous reconstructions may arise when a noisy data set is used to estimate the kernel **G** in Equation [1]. In practice, we used the data from the NWS scan to estimate the kernel **G**, because it has much higher SNR than WS data. However, the SNR of data without using the DC constraint did not show a strong difference between the peripheral and central regions (Table 1). There is no evidence that higher SNR gain using the DC constraint in the peripheral region than in the central region is related to the estimation of kernel **G**.

Another limitation of our method is related to the source of noise. The noise observed in MR originates from two main sources: the dielectric imaged object (brain) and the receiver coil element. Because noise from a different receiver coil would exhibit inconsistent behavior, the coil noise can be reduced by the DC algorithm. However, the noise from the brain would show a consistent pattern for neighboring coil elements. Body noise cannot be suppressed by the DC algorithm. Given that with the spatial resolution (mm–cm) at 3 T the MR noise is likely dominated by the body noise, the DC algorithm could perhaps achieve rather limited improvements. This may be the reason that fluctuating patterns shown in the 'noise' spectra, which supposedly contain only noise, only showed limited change even after DC processing (Fig. 2).

Our framework used the Tikhonov regularization framework to reconstruct images. This work has been studied extensively in pMRI (16,18,35). The proposed reconstruction algorithm can also incorporate an image sparsity feature in order to further suppress noise. This is closely related to the compressed sensing MRI (28). We expect that as the cost function in Equation [2] further incorporates the L-1 norm of a 'sparse' image (via, e.g., spatial differentiation or wavelet transformation), the noise in the reconstructed image may be further reduced. This will be the topic of our subsequent studies.

In conclusion, our experimental results suggest that the carefully optimized combination of MRSI data from a coil array can save around 70% of scanning time to obtain a similar image and spectra SNR using $\lambda=5$. The conclusion is drawn in the consideration of performance of spectral quality from CRLBs, CVs and RMS errors. In this study, we only demonstrated that the DC constraint can be used to suppress noise in multichannel MRSI. We expect that the DC process can also work in other experiments suffering from low SNR, such as functional brain imaging, perfusion imaging and low-field MRI (31).

Acknowledgements

This study was supported by grants from the Minister of Science and Technology, Taiwan (MOST 101-2320-B-004-001-MY2, MOST 103-2420-H-004-003-MY2, 102-2410-H-010-004-MY2, NSC 101-2628-B-002-005-MY3, MOST 103-2628-B-002-002-MY3, MOST 104-2314-B-002-238), the Ministry of Economic Affairs, Taiwan (100-EC-17-A-19-S1-175), the Ministry of Health and Welfare, Taiwan (MOHW103-TDU-PB-211-000026), the National Health Research Institute, Taiwan (NHRI-EX103-10247EI), the Finland Distinguished Professor (FiDiPro) program (TEKES) and the

Academy of Finland. The authors thank Taiwan Mind and Brain Imaging Center (TMBIC) for instrument availability for this work. TMBIC is supported by the Ministry of Science and Technology, Taiwan.

REFERENCES

1. Mansfield P. Spatial mapping of the chemical shift in NMR. Magn. Reson. Med. 1984; 1(3): 370–386.
2. Adalsteinsson E, Irarrazabal P, Topp S, Meyer C, Macovski A, Spielman DM. Volumetric spectroscopic imaging with spiral-based *k*-space trajectories. Magn. Reson. Med. 1998; 39(6): 889–898.
3. Tsai SY, Otazo R, Posse S, Lin YR, Chung HW, Wald LL, Wiggins GC, Lin FH. Accelerated proton echo planar spectroscopic imaging (PEPSI) using GRAPPA with a 32-channel phased-array coil. Magn. Reson. Med. 2008; 59(5): 989–998.
4. Lin FH, Tsai SY, Otazo R, Caprihan A, Wald LL, Belliveau JW, Posse S. Sensitivity-encoded (SENSE) proton echo-planar spectroscopic imaging (PEPSI) in the human brain. Magn. Reson. Med. 2007; 57(2): 249–257.
5. Tsai SY, Lin YR, Wang WC, Niddam DM. Short- and long-term quantitation reproducibility of brain metabolites in the medial wall using proton echo planar spectroscopic imaging. Neuroimage 2012; 63(3): 1020–1029.
6. Maudsley AA, Domenig C, Sheriff S. Reproducibility of serial whole-brain MR spectroscopic imaging. NMR Biomed. 2010; 23(3): 251–256.
7. Gottschalk M, Lamalle L, Segebarth C. Short-*TE* localised ^{1}H MRS of the human brain at 3 T: quantification of the metabolite signals using two approaches to account for macromolecular signal contributions. NMR Biomed. 2008; 21(5): 507–517.
8. Tsai SY, Posse S, Lin YR, Ko CW, Otazo R, Chung HW, Lin FH. Fast mapping of the T_2 relaxation time of cerebral metabolites using proton echo-planar spectroscopic imaging (PEPSI). Magn. Reson. Med. 2007; 57(5): 859–865.
9. Niddam DM, Tsai SY, Lin YR. Statistical mapping of metabolites in the medial wall of the brain: a proton echo planar spectroscopic imaging study. Hum. Brain Mapp. 2015; 36(3): 852–861.
10. Maudsley AA, Govind V, Arheart KL. Associations of age, gender and body mass with 1H MR-observed brain metabolites and tissue distributions. NMR Biomed. 2012; 25(4): 580–593.
11. Sabati M, Zhan J, Govind V, Arheart KL, Maudsley AA. Impact of reduced *k*-space acquisition on pathologic detectability for volumetric MR spectroscopic imaging. J. Magn. Reson. Imaging 2014; 39(1): 224–234.
12. Otazo R, Tsai SY, Lin FH, Posse S. Accelerated short-TE 3D proton echo-planar spectroscopic imaging using 2D-SENSE with a 32-channel array coil. Magn. Reson. Med. 2007; 58(6): 1107–1116.
13. Dydak U, Pruessmann KP, Weiger M, Tsao J, Meier D, Boesiger P. Parallel spectroscopic imaging with spin-echo trains. Magn. Reson. Med. 2003; 50(1): 196–200.
14. Sodickson DK, Manning WJ. Simultaneous acquisition of spatial harmonics (SMASH): fast imaging with radiofrequency coil arrays. Magn. Reson. Med. 1997; 38(4): 591–603.
15. Pruessmann KP, Weiger M, Scheidegger MB, Boesiger P. SENSE: sensitivity encoding for fast MRI. Magn. Reson. Med. 1999; 42(5): 952–962.
16. Lin FH, Wang FN, Ahlfors SP, Hamalainen MS, Belliveau JW. Parallel MRI reconstruction using variance partitioning regularization. Magn. Reson. Med. 2007; 58(4): 735–744.
17. Collins CM, Liu W, Swift BJ, Smith MB. Combination of optimized transmit arrays and some receive array reconstruction methods can yield homogeneous images at very high frequencies. Magn. Reson. Med. 2005; 54(6): 1327–1332.
18. Lin FH, Kwong KK, Belliveau JW, Wald LL. Parallel imaging reconstruction using automatic regularization. Magn. Reson. Med. 2004; 51(3): 559–567.
19. Martini N, Santarelli MF, Giovannetti G, Milanesi M, De Marchi D, Positano V, Landini L. Noise correlations and SNR in phased-array MRS. NMR Biomed. 2010; 23(1): 66–73.
20. Huang F, Lin W, Bornert P, Li Y, Reykowski A. Data convolution and combination operation (COCOA) for motion ghost artifacts reduction. Magn. Reson. Med. 2010; 64(1): 157–166.
21. Fautz HP, Honal M, Saueressig U, Schafer O, Kannengiesser SA. Artifact reduction in moving-table acquisitions using parallel imaging and multiple averages. Magn. Reson. Med. 2007; 57(1): 226–232.
22. Bydder M, Atkinson D, Larkman DJ, Hill DL, Hajnal JV. SMASH navigators. Magn. Reson. Med. 2003; 49(3): 493–500.
23. Atkinson D, Larkman DJ, Batchelor PG, Hill DL, Hajnal JV. Coil-based artifact reduction. Magn. Reson. Med. 2004; 52(4): 825–830.
24. Winkelmann R, Bornert P, Dossel O. Ghost artifact removal using a parallel imaging approach. Magn. Reson. Med. 2005; 54(4): 1002–1009.
25. Nana R, Hu X. Data consistency criterion for selecting parameters for *k*-space-based reconstruction in parallel imaging. Magn. Reson. Imaging 2010; 28(1): 119–128.
26. Tsai SY, Wang WC, Lin YR. Comparison of sagittal and transverse echo planar spectroscopic imaging on the quantification of brain metabolites. J. Neuroimaging 2015; 25(2): 167–174.
27. Griswold MA, Jakob PM, Heidemann RM, Nittka M, Jellus V, Wang J, Kiefer B, Haase A. Generalized autocalibrating partially parallel acquisitions (GRAPPA). Magn. Reson. Med. 2002; 47(6): 1202–1210.
28. Lustig M, Pauly JM. SPIRiT: iterative self-consistent parallel imaging reconstruction from arbitrary *k*-space. Magn. Reson. Med. 2010; 64(2): 457471.
29. Lin FH. Multidimensionally encoded magnetic resonance imaging. Magn. Reson. Med. 2013; 70(1): 86–96.
30. Lin FH, Witzel T, Schultz G, Gallichan D, Kuo WJ, Wang FN, Hennig J, Zaitsev M, Belliveau JW. Reconstruction of MRI data encoded by multiple nonbijective curvilinear magnetic fields. Magn. Reson. Med. 2012; 68(4): 1145–1156.
31. Lin FH, Vesanen PT, Hsu YC, Nieminen JO, Zevenhoven KC, Dabek J, Parkkonen LT, Simola J, Ahonen AI, Ilmoniemi RJ. Suppressing multichannel ultra-low-field MRI measurement noise using data consistency and image sparsity. PLoS One 2013; 8(4e61652).
32. Gasparovic C, Song T, Devier D, Bockholt HJ, Caprihan A, Mullins PG, Posse S, Jung RE, Morrison LA. Use of tissue water as a concentration reference for proton spectroscopic imaging. Magn. Reson. Med. 2006; 55(6): 1219–1226.
33. Govindaraju V, Young K, Maudsley AA. Proton NMR chemical shifts and coupling constants for brain metabolites. NMR Biomed. 2000; 13(3): 129–153.
34. Roemer PB, Edelstein WA, Hayes CE, Souza SP, Mueller OM. The NMR phased array. Magn. Reson. Med. 1990; 16(2): 192–225.
35. Lin FH, Huang TY, Chen NK, Wang FN, Stufflebeam SM, Belliveau JW, Wald LL, Kwong KK. Functional MRI using regularized parallel imaging acquisition. Magn. Reson. Med. 2005; 54(2): 343–353.